PHOTONICS Research

Polarization-independent multimode interference coupler with anisotropy-engineered bricked metamaterial

Carlos Pérez-Armenta,[1,*] Alejandro Ortega-Moñux,[1] José Manuel Luque-González,[1] Robert Halir,[1,2] Pedro J. Reyes-Iglesias,[1] Jens Schmid,[3] Pavel Cheben,[3] Íñigo Molina-Fernández,[1,2] and J. Gonzalo Wangüemert-Pérez[1,2]

[1]Telecommunication Research Institute (TELMA), Universidad de Málaga, CEI Andalucía TECH, E.T.S.I. Telecomunicación, 29010 Málaga, Spain
[2]Bionand Center for Nanomedicine and Biotechnology, Parque Tecnológico de Andalucía, Málaga 29590, Spain
[3]National Research Council Canada, Ottawa, Ontario K1A 0R6, Canada
*Corresponding author: cpa@ic.uma.es

Received 26 October 2021; revised 22 January 2022; accepted 1 February 2022; posted 2 February 2022 (Doc. ID 446932); published 11 March 2022

Many applications, including optical multiplexing, switching, and detection, call for low-cost and broadband photonic devices with polarization-independent operation. While the silicon-on-insulator platform is well positioned to fulfill most of these requirements, its strong birefringence hinders the development of polarization-agnostic devices. Here we leverage the recently proposed bricked metamaterial topology to design, for the first time, to our knowledge, a polarization-independent 2 × 2 multimode interference coupler using standard 220 nm silicon thickness. Our device can be fabricated with a single etch step and is optimized for the O-band, covering a wavelength range of 160 nm with excess loss, polarization-dependent loss, and imbalance below 1 dB and phase errors of less than 5°, as demonstrated with full three-dimensional finite-difference time-domain simulations.

https://doi.org/10.1364/PRJ.446932

1. INTRODUCTION

Silicon-on-insulator (SOI) is a prominent platform for the development of photonic integrated circuits (PICs). The high refractive index contrast between silicon and silicon dioxide enables the development of compact integrated photonic devices. Combined with CMOS-compatible fabrication, these benefits are driving the growth of the silicon photonic transceiver market [1] as well as research in biochemical sensing [2], lidars [3], quantum information processing [4], and other important applications. However, devices implemented in SOI typically suffer from high birefringence, especially for the widely used 220 nm waveguide thickness [1]. Thus, PICs often work for only one polarization at the operating wavelength.

Since the light coming from an optical fiber is usually in a random state of polarization, some applications require the use of polarization-independent devices. This is the case, for example, when designing building blocks for passive optical networks (PONs). Furthermore, standardization groups from ITU-T and IEEE are working on increasing the PON line rate by operating in the O-band where the low chromatic dispersion of optical fibers reduces intersymbol interference [5]. The design of transceivers to operate in the O-band is also of great interest in metro and access networks to provide point-to-point interfaces with the high capacity and low latency required to support radio access networks for 5G and beyond [6]. On the other hand, a widely used solution to increase receiver sensitivity, and therefore to enhance the optical power budget link, is to properly combine the incoming signal with a local oscillator in an optical hybrid before beating them in photodiodes. As an alternative to the conventional intradyne coherent receiver assisted by digital signal processing, much simpler reception schemes for PON have been recently proposed [7,8]. In these approaches, the availability of integrated polarization-independent hybrids would enable the implementation of low-cost and compact transceivers.

Approaches for implementing polarization-independent devices include using square waveguides [9], employing polarization diversity schemes at the cost of doubling the device footprint and additional insertion loss [10], or optimizing the device to match the behavior of both transverse electric (TE) and transverse magnetic (TM) polarizations [11]. Examples of the latter approach include power splitters using cascaded bent directional couplers [12], mode-evolution directional couplers

[13], optimized tapered couplers [14], broadband power dividers with modal-engineered slot waveguides [15], or filters using Bragg gratings [16,17].

Multimode interference (MMI) devices are key building blocks in PICs, as they can be used to build different components such as power splitters, Mach–Zehnder interferometers, or coherent receivers [18,19]. MMIs utilize wide and highly birefringent waveguides typically optimized for TE modes, making it difficult to achieve polarization-insensitive behavior. A strategy for making polarization-independent MMI devices is based on using a particular MMI width for which the TE and TM self-imaging distances are the same [20,21]. Nevertheless, this approach is not effective for the 220 nm thick SOI platform, since the necessary waveguide dimensions would be too small for proper multimode imaging. In Ref. [20], the minimum studied SOI thickness was 300 nm, for which the optimal width was found to be as small as 2 μm, hence difficult to scale down to 220 nm SOI. An additional silicon nitride overlay (SiN-on-SOI) [22] can be used to implement polarization-insensitive MMI couplers, taking advantage of the lower index contrast, at the cost of an increased fabrication complexity. Yet another strategy to achieve polarization-insensitive MMI couplers is using subwavelength grating (SWG) metamaterials. SWGs, since their first demonstration in silicon waveguides [23–27], have been used as a powerful tool for overcoming performance limitations of conventional silicon-based integrated photonic devices [28–30]. Various polarization-agnostic devices designed through SWG engineering have been demonstrated, including directional couplers [31–33], grating couplers [34], and non-birefringent tilted SWG waveguides [35]. A 1 × 2 MMI power splitter using an SWG slot and a silicon layer thickness of 250 nm has also been proposed [36].

Recently, a brick-patterned subwavelength metamaterial has been demonstrated [37], enabling engineering of the anisotropy of SWGs. Furthermore, it preserves a single etch step process and Manhattan-like geometry, thereby facilitating wafer-scale fabrication. In this work, we explore the properties of bricked SWG waveguides to design, for the first time, a polarization-insensitive 2 × 2 90° MMI coupler for the 220 nm SOI platform. We engineer the geometry of the waveguide to cover the wavelength ranges of 1.26–1.42 μm, with excess loss (EL), polarization-dependent loss (PDL), and imbalance (IB) below 1 dB and phase error (PE) lower than 5°, operating simultaneously for both TE and TM polarizations.

The paper is organized as follows. In Section 2, we summarize the working principle of the proposed device. In Section 3, a two-dimensional (2D) anisotropic model for the bricked SWG waveguide is presented. In Section 4, the design methodology is described, and in Section 5, the simulation results are discussed. Finally, conclusions are drawn in Section 6.

2. BRICKED METAMATERIAL MMI WORKING PRINCIPLE

The proposed device is shown in Fig. 1(a). It is a 2 × 2 MMI with the multimode region comprising a bricked SWG metamaterial, including the corresponding transitions between the interconnecting conventional silicon (Si) waveguide of width w_{in} and the bricked SWG input/output access waveguides of width w_a. As shown in Fig. 1(c), the brick pattern includes two periodicities: the first with a period $\Lambda_z = a_z + b_z$ and duty cycle (DC) $\mathrm{DC}_z = a_z/\Lambda_z$ along the propagation direction (z), and the second with a period $\Lambda_x = a_x + b_x$ and $\mathrm{DC}_x = a_x/\Lambda_x$ in the transversal direction (x). The longitudinal displacement d_z shapes the bricked geometry and significantly contributes to the metamaterial anisotropy. For $d_z = 0$, the structure is a conventional SWG waveguide, whereas for $\mathrm{DC}_z < d_z/\Lambda_z < 1 - \mathrm{DC}_z$, the silicon segments are isolated from each other. The width and length of the multimode waveguide are w_{MMI} and $L_{\mathrm{MMI}} = N_{\mathrm{MMI}}\Lambda_z$, respectively, where N_{MMI} is the number of SWG periods. Wire-to-bricked SWG tapers, shown schematically in Fig. 1(b), are located at the input and output ports of the MMI. The tapering is used to widen the input access waveguides as in conventional MMI devices to ensure that only lower-order modes are excited, while at the same time to adapt the bricked SWG multimode waveguide to the interconnecting strip waveguides. The device is designed for the SOI platform, with a silicon core thickness of $h = 220$ nm and silicon dioxide (SiO_2) upper and lower cladding. The corresponding refractive indices are $n_{\mathrm{Si}} = 3.503$ and $n_{\mathrm{SiO_2}} = 1.466$ at the wavelength of 1.31 μm.

The operation of the MMI coupler is governed by the self-imaging effect [18]. For a general interference case, the distance at which the first two-fold image of the input field profile is formed is

$$L_{\mathrm{MMI}} = \frac{3}{2}L_\pi, \tag{1}$$

where L_π is the beat length of the two lowest-order modes given by

$$L_\pi = \frac{\pi}{\beta_0 - \beta_1}. \tag{2}$$

In Eq. (2), β_0 and β_1 are the propagation constants of the two lowest-order modes of the multimode region for a given polarization, TE or TM. Ideally, when the MMI length is given by Eq. (1), a signal entering port 1 [Fig. 1(a)] should be equally split between ports 2 and 3 with a relative phase shift of 90°. For a conventional MMI, the beat length substantially differs for TE and TM polarizations. The primary objective of this work is to optimize the bricked SWG core to achieve identical beat lengths for both polarizations, $L_\pi^{(\mathrm{TE})} = L_\pi^{(\mathrm{TM})}$, thus obtaining a polarization-insensitive device. For that purpose, the longitudinal displacement d_z of the silicon blocks of size $a_x \times a_z$ is used. This parameter is crucial for controlling the anisotropy of the bricked SWG waveguides. In Ref. [37], it was shown that TE modes are significantly more sensitive to longitudinal displacement d_z than TM modes. Here we leverage this unique advantage of bricked SWG topology to design a polarization-insensitive MMI.

3. 2D ANISOTROPIC MODEL OF THE BRICKED SWG MMI

MMI couplers implemented in 220 nm SOI waveguides are single mode in the out-of-plane (y) direction. Therefore, an analytic formula for the beat length of a homogeneous MMI can be obtained based on paraxial approximation using

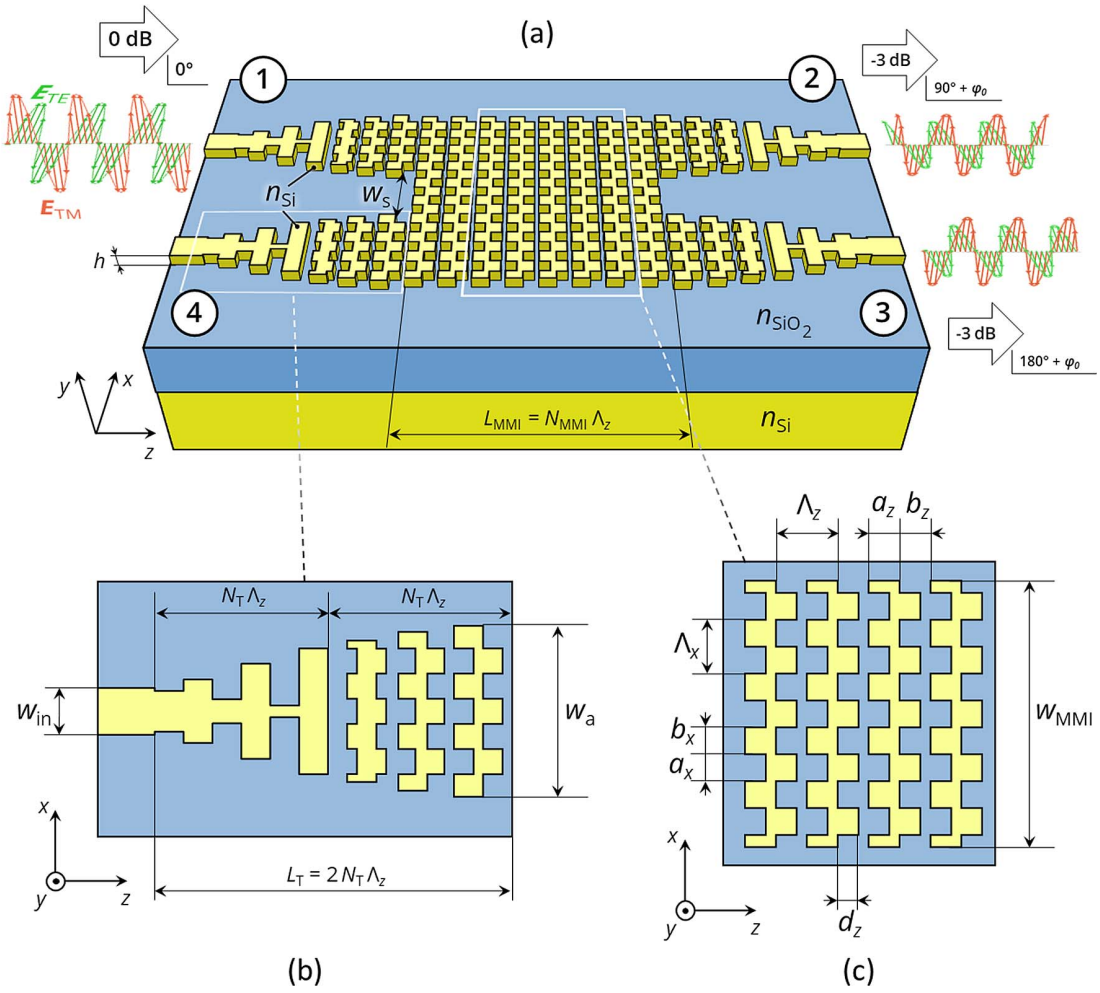

Fig. 1. (a) Schematic of the proposed polarization-insensitive 2 × 2 MMI (SiO_2 cladding is not shown for clarity). (b) Top view of the taper from input silicon wire to bricked SWG waveguide. (c) Top view of the bricked SWG multimode waveguide.

equivalent 2D waveguides, e.g., by the effective index method (EIM) [18]. In Ref. [38], a generalization of the EIM was proposed to characterize anisotropic SWG multimode waveguides for TE modes. In this section, we generalize the procedure outlined in Ref. [38] by extending it to TM polarization, and apply this new model to the bricked SWG topology.

The in-plane (TE) modes of a slab waveguide with an anisotropic core obey the dispersion relation [38]

$$\left(\frac{k_{x,m}^{(\mathrm{TE})}}{n_{zz}}\right)^2+\left(\frac{\beta_m^{(\mathrm{TE})}}{n_{xx}}\right)^2=\left(\frac{2\pi}{\lambda}\right)^2, \tag{3}$$

where $k_{x,m}^{(\mathrm{TE})}=m\pi/w_{e,\mathrm{TE}}$ is the x component of the mth TE mode wave vector, $w_{e,\mathrm{TE}}$ is the effective width of the fundamental TE mode, $\beta_m^{(\mathrm{TE})}$ is the propagation constant of the mth TE mode, n_{ii}^2 is the i component of the electric permittivity tensor, and λ is the vacuum wavelength. The n_{xx} and n_{zz} terms can be calculated by solving the unit cell of Fig. 2(a), e.g., using the rigorous three-dimensional (3D) full-vectorial MIT Photonic Bands (MPB) tool [39]. As outlined in Fig. 2(a), to obtain n_{xx} and n_{zz}, the effective index of the fundamental TE mode is calculated when propagating in the z and x directions, respectively. Note that this structure is infinitely periodic in the x and z directions. Then, a first-order Taylor expansion in Eq. (3) yields the following approximate beat length:

$$L_\pi^{(\mathrm{TE})}\approx\frac{4w_{e,\mathrm{TE}}^2}{3\lambda}\frac{n_{zz}^2}{n_{xx}}. \tag{4}$$

Here we extend this 2D anisotropic model to TM polarization by incorporating two additional refractive index components, n_{yy} and n'_{yy}. These are also calculated using MPB, as generally represented in Fig. 2(a). To find n_{yy} and n'_{yy}, the fundamental TM mode effective index is calculated for propagation along the z and x directions, respectively. By analogy with Eq. (4), the beat length of TM modes is given by

$$L_\pi^{(\mathrm{TM})}\approx\frac{4w_{e,\mathrm{TM}}^2}{3\lambda}\frac{(n'_{yy})^2}{n_{yy}}. \tag{5}$$

A polarization-independent operation of the MMI is achieved provided that the corresponding beat lengths of TE and TM polarizations are designed to be identical, i.e., $w_{e,\mathrm{TE}}^2 n_{zz}^2/n_{xx}=w_{e,\mathrm{TM}}^2(n'_{yy})^2/n_{yy}$.

In the design example of Fig. 2(b), the n_{ii} components of a bricked SWG waveguide with $h=220$ nm, $\Lambda_x=200$ nm,

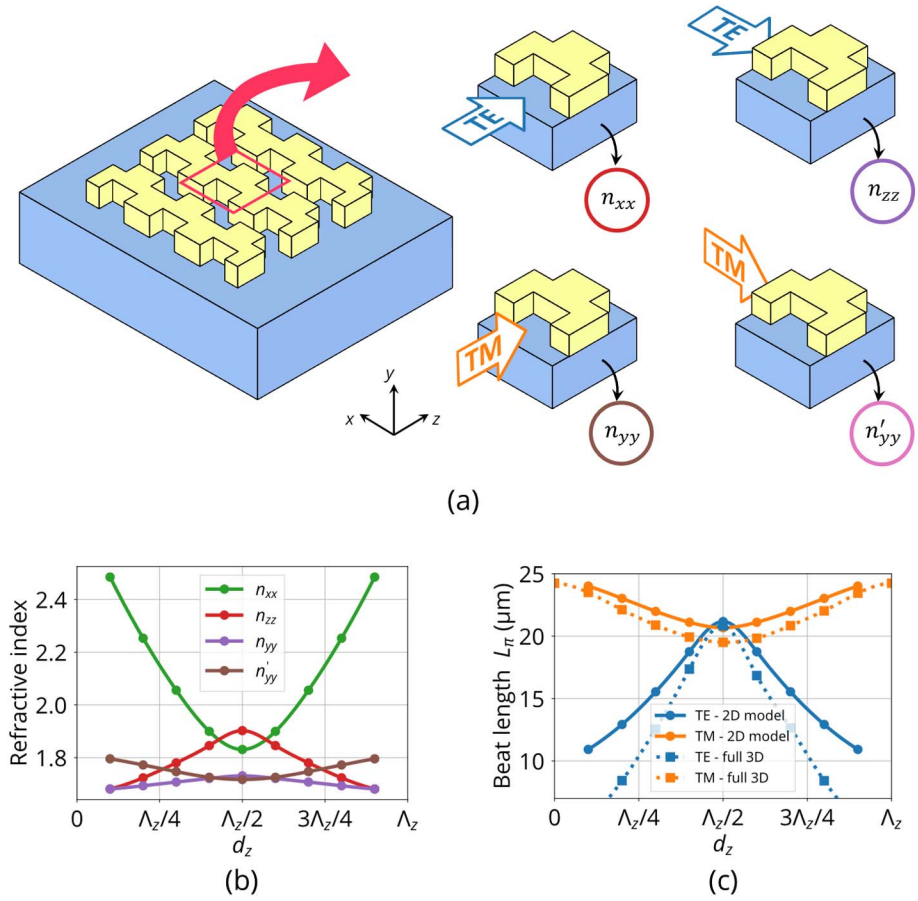

Fig. 2. (a) Procedure employed for modeling the bricked SWG. (b) Calculated refractive index components for a bricked SWG waveguide with $h = 220$ nm, $\Lambda_x = 200$ nm, $\mathrm{DC}_x = 50\%$, $\Lambda_z = 240$ nm, and $\mathrm{DC}_z = 50\%$ at the wavelength $\lambda = 1.31$ μm. (c) Beat length for $w_{\mathrm{MMI}} = 3$ μm using the 2D anisotropic model (solid curves) and full 3D simulations (dotted curves).

$\mathrm{DC}_x = 50\%$, $\Lambda_z = 240$ nm, and $\mathrm{DC}_z = 50\%$ are obtained for a central wavelength of $\lambda = 1.31$ μm. Using these results, along with the effective width [18] corresponding to the waveguide width of $w_{\mathrm{MMI}} = 3$ μm for both polarizations in Eqs. (4) and (5), yields the beat lengths shown in Fig. 2(c) (solid lines). Furthermore, a bricked SWG waveguide with the same parameters as the unit cell and the same width, $w_{\mathrm{MMI}} = 3$ μm, is simulated in 3D with the MPB solver for the two first modes of each polarization. The calculated propagation constants are substituted in Eq. (2) to obtain the corresponding beat lengths. Results are shown in Fig. 2(c), as dotted curves. We observe that the 2D model correctly follows the trend confirmed by the full 3D simulations using MPB, which predicts the optimum shifting value $d_z \approx \Lambda_z/2$ to obtain $L_\pi^{(\mathrm{TE})} = L_\pi^{(\mathrm{TM})}$. The accuracy of the simplified 2D model is highly dependent on the shifting and polarization, but it gives accurate results near the design point. The error in the 2D estimation of L_π at $d_z = \Lambda_z/2$ is negligible for TE polarization, and about 1 μm for TM polarization. It is also observed that for $d_z = 0$, which corresponds to a conventional SWG waveguide (without bricking), the difference between TE and TM beat lengths is maximum. A grid resolution of 128 pixels/μm and cell size of 6 μm × 4 μm × Λ_z were used for the 3D waveguide simulation, while for the 2D anisotropic model, the cell size of Λ_x × 4 μm × Λ_z was employed. The sweep of Fig. 2(c) lasted 2 h for the 3D simulation waveguide, while for 2D approximation, the permittivity tensor was calculated in less than 90 s (running on a single core of an Intel Xeon Gold 6242R at 3.10 GHz), yielding about two orders of magnitude difference in simulation time. Therefore, using our 2D anisotropic model, a good design starting point can be obtained, substantially reducing the optimization time for the full 3D structure.

4. DESIGN OF THE BRICKED SWG MULTIMODE WAVEGUIDE

The geometrical parameters of the central multimode waveguide are optimized using the procedure outlined in Fig. 3(a). The multimode waveguide width is initially chosen as $w_{\mathrm{MMI}} = 3$ μm to ensure that it supports a sufficient number of modes without substantially increasing the waveguide length, as the latter increases with w_{MMI}^2. The DC in z direction is $\mathrm{DC}_z = 50\%$, and the transversal periodicity is set to $\Lambda_x = 200$ nm and $\mathrm{DC}_x = 50\%$, to maintain a minimum feature size of 100 nm and work far from Bragg resonance. More details on this aspect are presented in Appendix A.

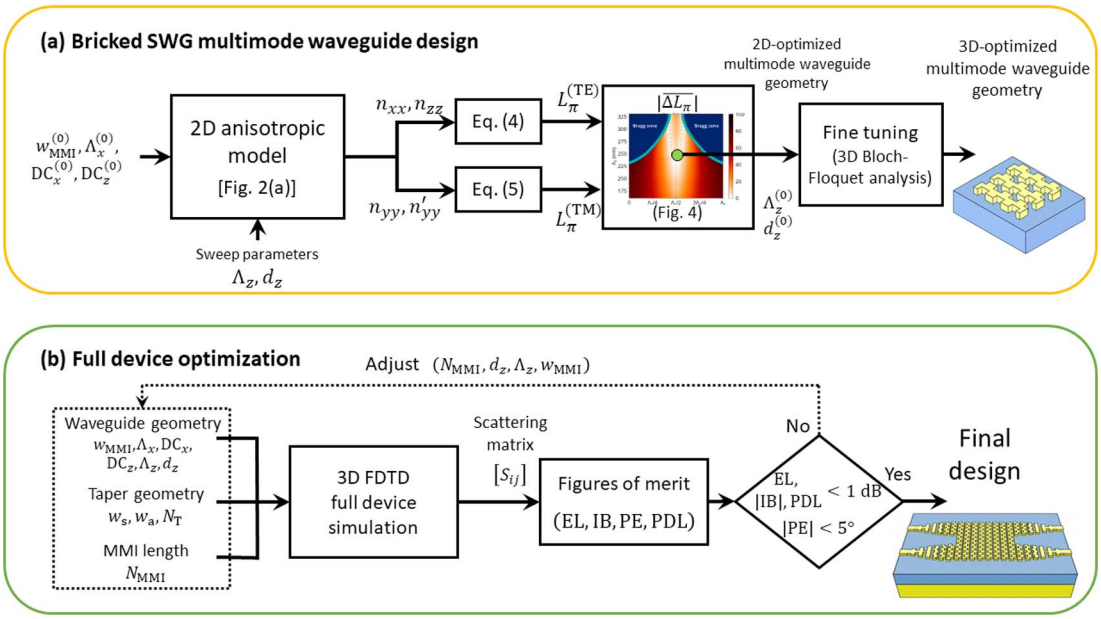

Fig. 3. Design methodology used in this work, comprising two main stages: (a) design of the bricked SWG multimode waveguide and (b) optimization of the complete device using a 3D-FDTD simulator.

To obtain the first design iteration, the SWG structure was simulated using the approximate 2D anisotropic model. Figure 4 shows a contour map of the relative difference between the beat lengths for TE and TM polarizations, defined as $\overline{\Delta L_\pi} = \Delta L_\pi / \overline{L_\pi}$, where $\Delta L_\pi = L_\pi^{(\mathrm{TE})} - L_\pi^{(\mathrm{TM})}$ and $\overline{L_\pi} = (L_\pi^{(\mathrm{TE})} + L_\pi^{(\mathrm{TM})})/2$. The parameter ΔL_π was calculated as a function of the longitudinal pitch Λ_z and the normalized shift d_z/Λ_z, for $\lambda = 1310$ nm. Some important observations on polarization effects are concluded from these results, as shown in Fig. 4: (i) for a given pitch Λ_x, there is a minimum Λ_z below which polarization insensitivity cannot be achieved,

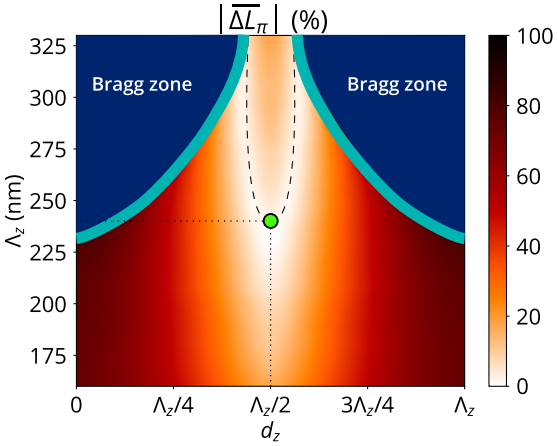

Fig. 4. Absolute value of the relative difference between TE and TM beat lengths $|\overline{\Delta L_\pi}| = |\Delta L_\pi / \overline{L_\pi}|$, where $\Delta L_\pi = L_\pi^{(\mathrm{TE})} - L_\pi^{(\mathrm{TM})}$ and $\overline{L_\pi} = (L_\pi^{(\mathrm{TE})} + L_\pi^{(\mathrm{TM})})/2$, calculated using the anisotropic 2D model. Simulation parameters of the unit cell are $h = 220$ nm, $\mathrm{DC}_z = \mathrm{DC}_x = 50\%$, $\Lambda_x = 200$ nm, and $\lambda = 1.31$ μm. The dashed line represents the points (d_z, Λ_z) for which $\overline{\Delta L_\pi} = 0$. The optimal parameters $\Lambda_z = 240$ nm and $d_z = \Lambda_z/2$ are marked with a green dot.

(ii) the optimal bricked shifting d_z is approximately $\Lambda_z/2$, and (iii) longer periods restrict the selection of d_z as the Bragg regime approaches the operation band. So, with a minimal computational effort, we choose $\Lambda_z = 240$ nm and $d_z = \Lambda_z/2$ as the initial design point, while the other structural parameters were set as stated above.

As the next step, we perform full-vectorial 3D simulations of the bricked SWG waveguide near this initial design point, to correct for the inaccuracy of the 2D model. Using MPB, we calculate the two lowest-order Floquet–Bloch modes of the multimode section. From the condition $L_\pi^{(\mathrm{TE})} = L_\pi^{(\mathrm{TM})}$ at $\lambda = 1.31$ μm, we obtain $\Lambda_z = 220$ nm and $d_z = 0.48\Lambda_z$. The beat length is then calculated using Eq. (2) to be 18 μm. The calculated curves for TE and TM beat lengths as a function of wavelength are shown in Fig. 5.

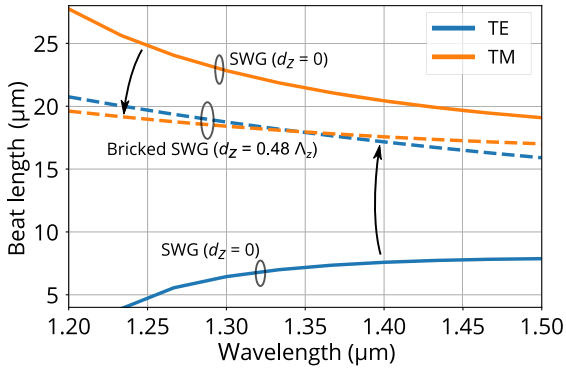

Fig. 5. Beat length as a function of wavelength obtained from 3D Floquet–Bloch simulations of the (bricked) SWG waveguide. Solid lines correspond to $d_z = 0$, while dashed lines correspond to $d_z = 0.48\Lambda_z$. Other geometrical parameters are: $w_{\mathrm{MMI}} = 3$ μm, $h = 220$ nm, $\Lambda_x = 200$ nm, $\mathrm{DC}_x = 50\%$, $\Lambda_z = 220$ nm, and $\mathrm{DC}_z = 50\%$.

Table 1. Optimized Design Parameters of Polarization Insensitive 2 × 2 MMI Coupler

Parameter	w_{MMI}	Λ_z (DC_z)	Λ_x (DC_x)	d_z	N_{MMI}	w_a	w_s	N_T
Value	2.9 μm	220 nm (50%)	200 nm (50%)	110 nm	121	1.2 μm	0.8 μm	21

5. DESIGN OF THE COMPLETE DEVICE

To complete the full design, the procedure outlined in Fig. 3(b) is applied. We first optimize the access ports and the transitions between the interconnecting waveguides and the bricked SWG waveguide. The width of the MMI access ports w_a is designed to ensure that only lower-order modes of the multimode waveguide are excited [38]. Subsequently, the separation between the MMI ports w_s is chosen to minimize the coupling between the access waveguides. The transition from the interconnecting single-mode waveguides of width $w_{\mathrm{in}} = 400$ nm to the access ports w_a is shown in Fig. 1(b). It is divided into two sections of N_T periods each, where the first one converts a photonic wire into an SWG waveguide and the second one progressively introduces the brick shifting. This design strategy effectively reduces Bragg reflections along the taper. Simulation of the full device is carried out using the 3D full-vectorial finite-difference time-domain (FDTD) open-source simulator Meep [40]. The simulation parameters used are a grid resolution of 128 pixels/μm and a simulation window size of 7 μm × 5 μm × L_z, where the length L_z depends on the MMI and taper lengths.

To assess the overall performance of the device, we calculated the EL [$\mathrm{EL} = -10\log(|S_{21}|^2 + |S_{31}|^2)$], IB [$\mathrm{IB} = 10\log|S_{31}/S_{21}|^2$], PE [$\mathrm{PE} = \arg(S_{31}/S_{21}) - 90^\circ$], and PDL [$\mathrm{PDL} = |\mathrm{EL}_{\mathrm{TE}} - \mathrm{EL}_{\mathrm{TM}}|$] from the S-parameters obtained by 3D FDTD simulations. Some of the device parameters (d_z, Λ_z, N_{MMI}, and w_{MMI}) were fine-tuned to optimize the performance of the device in terms of EL, IB, PE, and PDL. The initial design point obtained from the first design stage [Fig. 3(a)] was good enough to require only minor adjustments in the second stage [Fig. 3(b)], so that no additional optimization routines to further optimize EL, IB, PE, and PDL were required. The optimized final design parameters are given in Table 1.

The optimized MMI performance is shown in Fig. 6. PDL is below 1 dB for the wavelength range of 1.24–1.45 μm and it is limited by TE polarization performance. This is consistent with the larger wavelength dependence of the beat length for TE polarization, as shown in Fig. 5. Both polarizations exhibit simultaneously IB below 1 dB from 1.19 μm to 1.42 μm, and PEs less than 5° (1.26–1.50 μm). The performance of the designed device is compared with other state-of-the-art polarization insensitive SOI-based MMI couplers in Table 2. Note that some of the cited works are 1 × 2 couplers, which are simpler devices and hence typically offer better performance than 2 × 2 90° MMI couplers. These results confirm that bricked SWG waveguides are highly effective in mitigating device PDL, allowing design of polarization-insensitive MMI couplers in 220 nm thick SOI waveguides.

Regarding fabrication tolerance, the robustness of the nominal design to fabrication deviations has been studied for in-plane over-etching and under-etching errors up to 20 nm as illustrated in the inset of Fig. 7(b). Figure 7 shows the center wavelength and bandwidth of the device as a function of the fabrication error δ, where $\delta < 0$ means over-etching and $\delta > 0$ under-etching, in the chip plane. We define the bandwidth of the device as the wavelength range in which PDL, EL, and |IB| are simultaneously below 1 dB and |PE| is less than 5°. It can be seen that for $|\delta| < 15$ nm, the MMI has a bandwidth greater than 100 nm for both polarizations. In addition, the center wavelength has a

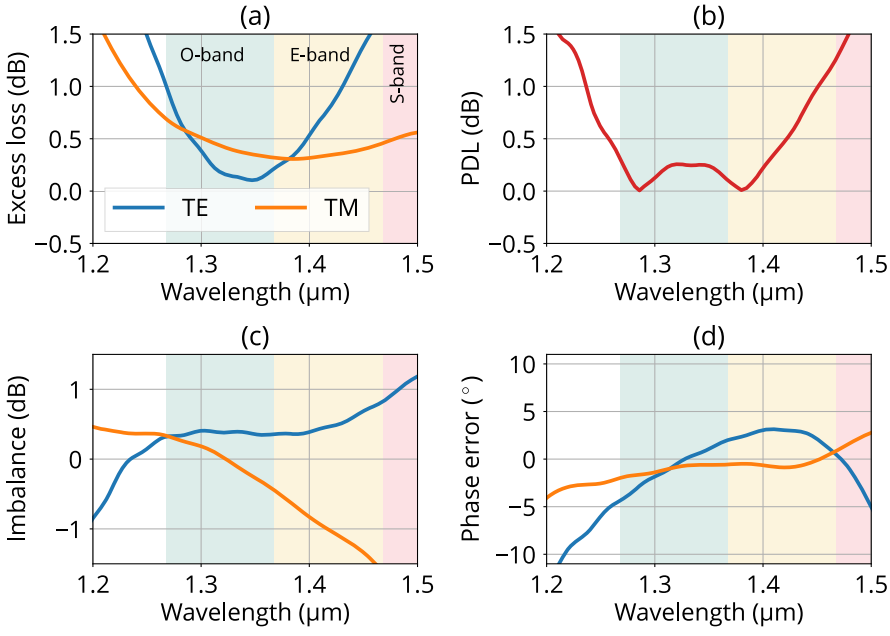

Fig. 6. Final design performance of the optimized polarization-independent 2 × 2 MMI.

Table 2. Comparison of Our Device with Other State-of-the-Art Polarization-Insensitive SOI-based MMI Couplers

Reference	Performance	λ_0	BW ($\Delta\lambda/\lambda_0$)	Type	Footprint	Si Thickness (nm)
[20]	EL < 1 dB	1550 nm	80 nm (5%)	1 × 2	3.9 μm × 15.3 μm	400
[36]	EL < 1 dB, |IB| < 1 dB, PDL < 0.1 dB	1550 nm	200 nm (13%)	1 × 2	2 μm × 7.7 μm	250
[21]	EL < 0.3 dB, |IB| < 0.7 dB	1550 nm	100 nm (6%)	2 × 2	2 μm × 14.4 μm	340
This work	**EL<1 dB, |IB|<1 dB, PDL<1 dB, |PE|<5°**	**1310 nm**	**160 nm (12%)**	**2 × 2**	**3 μm × 35.9 μm**	**220**

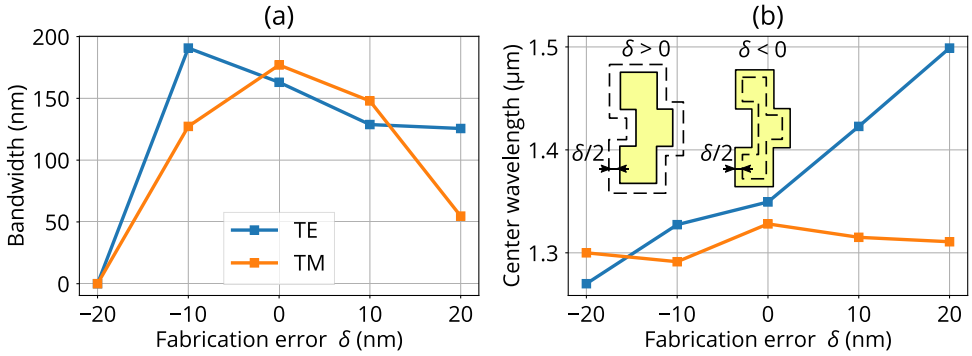

Fig. 7. Dependence of the bandwidth and center wavelength of the MMI on fabrication error δ. The bandwidth is defined as the wavelength range in which PDL, EL, and |IB| are simultaneously below 1 dB, and |PE| is less than 5°. The inset shows the effect on the in-plane geometry of positive and negative values of δ. The original geometry (top view, i.e., in the chip plane) is represented with a continuous line, while the over/under-etched geometry is represented with a dashed line.

small dependence on δ for TM polarization. Although TE center wavelength is heavily shifted when $\delta > 0$, it is robust to fabrication errors of $\delta = -10$ nm. This asymmetric behavior with respect to δ can be taken into account by introducing a small bias in the mask definition stage. We also studied a ±2% variation of the grating periods (Λ_x, Λ_z), which resulted in a ±30 nm detuning of the device wavelength response.

6. CONCLUSION

We have proposed the first polarization-independent 2 × 2 MMI coupler in a 220 nm SOI platform. Our design leverages the concept of bricked SWG metamaterial waveguide engineering. Our optimized MMI device design features sub-decibel level of insertion loss, PDL, and IB, and PEs under 5° in the wavelength range of 1.26–1.42 μm. This is an unprecedented design performance for a 2 × 2 MMI in a standard 220 nm SOI platform. The 2D model and design methodology proposed in this work is general and indeed can be readily applied to MMIs with larger numbers of ports. We believe that our design strategy based on anisotropy engineering using bricked SWG metamaterial waveguides opens promising prospects for development of polarization-insensitive integrated photonic components and devices.

APPENDIX A: INFLUENCE OF BRICKED SWG PITCH AND DUTY CYCLE ON MMI PERFORMANCE

In Section 4, we fixed three geometrical parameters of the bricked SWG core to $\Lambda_x = 200$ nm, and $DC = DC_x = DC_z = 50\%$. Here we justify this choice by considering different periods and DCs.

Figure 8 shows the contour maps of $|\overline{\Delta L_\pi}|$ as a function of the longitudinal pitch size (Λ_z) and bricked shifting (d_z) for different values of DCs ($DC_x = DC_z = DC = 40\%, 50\%, 60\%$) and transversal periods ($\Lambda_x = 200$ nm, 250 nm, 300 nm). As described in Section 4, such contour maps can be obtained following the procedure of Fig. 3(a). Figure 8(d) corresponds to the same case simulated in Fig. 4, where the chosen design point is marked with a green dot ($\Lambda_x = 200$ nm, $\Lambda_z = 240$ nm, $DC = 50\%$, $d_z = \Lambda_z/2$).

An analysis of the results of Fig. 8 yields the following conclusions: (i) the Bragg zone grows for DC increasing above 50%, resulting in a reduction of the design space, (ii) the possible design solutions (where $\Delta L_\pi = 0$) move towards the Bragg zone when DC is reduced below 50%, (iii) although increasing the period relaxes minimum feature size constraints, it also shifts the polarization-independent designs closer to the Bragg zone [see Fig. 8(e)] or even makes them impossible [see Figs. 8(b), 8(c), 8(f), 8(h), and 8(i)].

Thus, increasing the grating pitch or shifting DC away from 50% will degrade the bandwidth of the device due to the proximity of the Bragg zone and the corresponding increase in backreflections. In addition, the proximity of the Bragg zone potentially increases the influence of disorder (jitter) for a given fabrication process [41]. Designing periodic devices with feature sizes greater than 100 nm indeed is more challenging at the O-band (1260–1360 nm) than at the C-band (1530–1565 nm), as the shorter wavelength requires the use of shorter periods to keep the Bragg resonance effect negligible. Therefore, the chosen preliminary design represents a good trade-off between keeping minimum feature size larger than 100 nm and ensuring that the Bragg zone is far from the operation band.

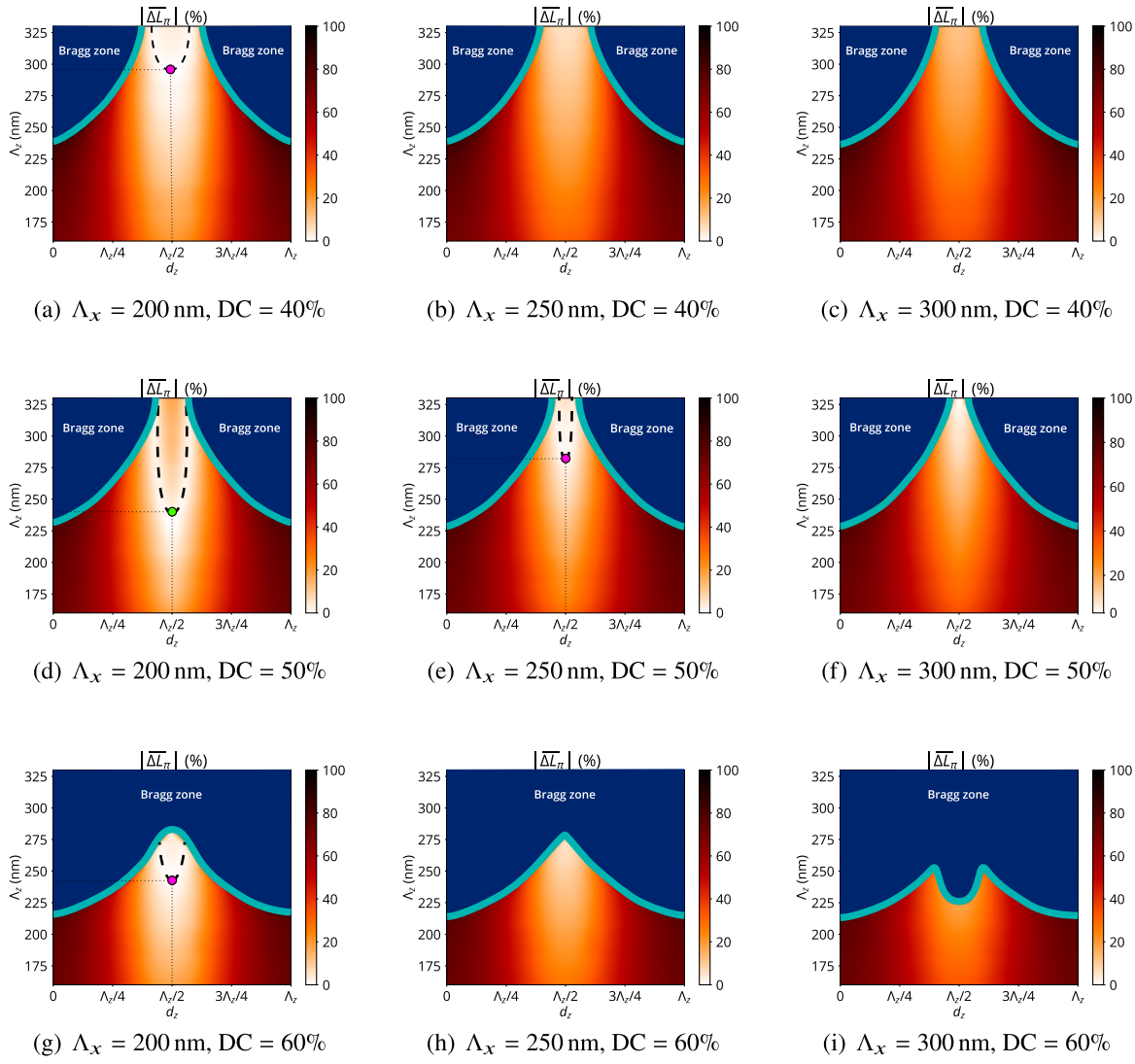

Fig. 8. Calculation of $|\overline{\Delta L_\pi}|$ as performed in Fig. 4 for different transversal periods Λ_x and duty cycles (DC = DC_x = DC_z) and the wavelength of $\lambda = 1310$ nm. The dashed line corresponds to $|\Delta L_\pi| = 0$. The design point is marked with a green dot in (d). For $\Lambda_x > 200$ nm or DC $\neq$ 50%, the design space for $|\overline{\Delta L_\pi}|$ is closer to the Bragg zone [see cases (a), (e), and (g)] or no solution can be found, as shown in (b), (c), (f), (h), and (i).

Funding. Ministerio de Economía y Competitividad (PID2019-106747RB-I00); Junta de Andalucía (P18-RT-1453, UMA-FEDERJA-158); Ministerio de Ciencia, Innovación y Universidades (FPU16/06762, FPU19/02408); Universidad de Málaga.

Disclosures. The authors declare no conflicts of interest.

Data Availability. Data underlying the results presented in this paper are not publicly available at this time but may be obtained from the authors upon reasonable request.

REFERENCES

1. A. Rahim, T. Spuesens, R. Baets, and W. Bogaerts, "Open-access silicon photonics: current status and emerging initiatives," Proc. IEEE **106**, 2313–2330 (2018).
2. E. Luan, H. Shoman, D. M. Ratner, K. C. Cheung, and L. Chrostowski, "Silicon photonic biosensors using label-free detection," Sensors **18**, 3519 (2018).
3. K. Y. Yang, J. Skarda, M. Cotrufo, A. Dutt, G. H. Ahn, M. Sawaby, D. Vercruysse, A. Arbabian, S. Fan, A. Alù, and J. Vučković, "Inverse-designed non-reciprocal pulse router for chip-based LiDAR," Nat. Photonics **14**, 369–374 (2020).
4. A. W. Elshaari, W. Pernice, K. Srinivasan, O. Benson, and V. Zwiller, "Hybrid integrated quantum photonic circuits," Nat. Photonics **14**, 285–298 (2020).
5. D. Zhang, D. Liu, X. Wu, and D. Nesset, "Progress of ITU-T higher speed passive optical network (50G-PON) standardization," J. Opt. Commun. Netw. **12**, D99–D108 (2020).
6. F. Saliou, P. Chanclou, L. A. Neto, G. Simon, J. Potet, M. Gay, L. Bramerie, and H. Debregeas, "Optical access network interfaces for 5G and beyond [Invited]," J. Opt. Commun. Netw. **13**, D32–D42 (2021).
7. M. S. Erkılınç, D. Lavery, K. Shi, B. C. Thomsen, P. Bayvel, R. I. Killey, and S. J. Savory, "Polarization-insensitive single-balanced photodiode coherent receiver for long-reach WDM-PONs," J. Lightwave Technol. **34**, 2034–2041 (2016).

8. M. S. Erkılınç, D. Lavery, K. Shi, B. C. Thomsen, R. I. Killey, S. J. Savory, and P. Bayvel, "Comparison of low complexity coherent receivers for UDWDM-PONs (λ-to-the-user)," J. Lightwave Technol. **36**, 3453–3464 (2018).
9. S. T. Lim, C. E. Png, E. A. Ong, and Y. L. Ang, "Single mode, polarization-independent submicron silicon waveguides based on geometrical adjustments," Opt. Express **15**, 11061–11072 (2007).
10. T. Barwicz, M. R. Watts, M. A. Popović, P. T. Rakich, L. Socci, F. X. Kärtner, E. P. Ippen, and H. I. Smith, "Polarization-transparent microphotonic devices in the strong confinement limit," Nat. Photonics **1**, 57–60 (2007).
11. D. Dai, L. Liu, S. Gao, D.-X. Xu, and S. He, "Polarization management for silicon photonic integrated circuits," Laser Photon. Rev. **7**, 303–328 (2013).
12. X. Chen, W. Liu, Y. Zhang, and Y. Shi, "Polarization-insensitive broadband 2 × 2 3 dB power splitter based on silicon-bent directional couplers," Opt. Lett. **42**, 3738–3740 (2017).
13. Y. Wang, L. Xu, H. Yun, M. Ma, A. Kumar, E. El-Fiky, R. Li, N. Abadíacalvo, L. Chrostowski, N. A. F. Jaeger, and D. V. Plant, "Polarization-independent mode-evolution-based coupler for the silicon-on-insulator platform," IEEE Photon. J. **10**, 4900410 (2018).
14. H. Li, W. Chen, P. Wang, S. Dai, Y. Liu, Q. Fu, J. Li, Y. Li, T. Dai, H. Yu, and J. Yang, "Compact and low-loss 1 × 3 polarization-insensitive optical power splitter using cascaded tapered silicon waveguides," Opt. Lett. **45**, 5596–5599 (2020).
15. D. González-Andrade, C. Lafforgue, E. Durán-Valdeiglesias, X. Le Roux, M. Berciano, E. Cassan, D. Marris-Morini, A. V. Velasco, P. Cheben, L. Vivien, and C. Alonso-Ramos, "Polarization- and wavelength-agnostic nanophotonic beam splitter," Sci. Rep. **9**, 3604 (2019).
16. D. Liu and D. Dai, "Silicon-based polarization-insensitive optical filter with dual-gratings," Opt. Express **27**, 20704–20710 (2019).
17. H. Yun, L. Chrostowski, and N. A. F. Jaeger, "Narrow-band, polarization-independent, transmission filter in a silicon-on-insulator strip waveguide," Opt. Lett. **44**, 847–850 (2019).
18. L. Soldano and E. Pennings, "Optical multi-mode interference devices based on self-imaging: principles and applications," J. Lightwave Technol. **13**, 615–627 (1995).
19. H. Guan, Y. Ma, R. Shi, X. Zhu, R. Younce, Y. Chen, J. Roman, N. Ophir, Y. Liu, R. Ding, T. Baehr-Jones, K. Bergman, and M. Hochberg, "Compact and low loss 90°; optical hybrid on a silicon-on-insulator platform," Opt. Express **25**, 28957–28968 (2017).
20. D. Dai and S. He, "Optimization of ultracompact polarization-insensitive multimode interference couplers based on Si nanowire waveguides," IEEE Photon. Technol. Lett. **18**, 2017–2019 (2006).
21. S. Wang and D. Dai, "Polarization-insensitive 2 × 2 thermo-optic Mach-Zehnder switch on silicon," Opt. Lett. **43**, 2531–2534 (2018).
22. S. Y. Siew, B. Li, F. Gao, H. Y. Zheng, W. Zhang, P. Guo, S. W. Xie, A. Song, B. Dong, L. W. Luo, C. Li, X. Luo, and G.-Q. Lo, "Review of silicon photonics technology and platform development," J. Lightwave Technol. **39**, 4374–4389 (2021).
23. P. Cheben, D.-X. Xu, S. Janz, and A. Densmore, "Subwavelength waveguide grating for mode conversion and light coupling in integrated optics," Opt. Express **14**, 4695–4702 (2006).
24. P. Cheben, S. Janz, D.-X. Xu, B. Lamontagne, A. Delage, and S. Tanev, "A broad-band waveguide grating coupler with a subwavelength grating mirror," IEEE Photon. Technol. Lett. **18**, 13–15 (2006).
25. J. H. Schmid, P. Cheben, S. Janz, J. Lapointe, E. Post, and D.-X. Xu, "Gradient-index antireflective subwavelength structures for planar waveguide facets," Opt. Lett. **32**, 1794–1796 (2007).
26. J. H. Schmid, P. Cheben, S. Janz, J. Lapointe, E. Post, A. Delâge, A. Densmore, B. Lamontagne, P. Waldron, and D.-X. Xu, "Subwavelength grating structures in silicon-on-insulator waveguides," Adv. Opt. Technol. **2008**, 685489 (2008).
27. P. J. Bock, P. Cheben, J. H. Schmid, A. Delâge, D.-X. Xu, S. Janz, and T. J. Hall, "Sub-wavelength grating mode transformers in silicon slab waveguides," Opt. Express **17**, 19120–19133 (2009).
28. R. Halir, A. Ortega-Moñux, D. Benedikovic, G. Z. Mashanovich, J. G. Wangüemert-Pérez, J. H. Schmid, I. Molina-Fernández, and P. Cheben, "Subwavelength-grating metamaterial structures for silicon photonic devices," Proc. IEEE **106**, 2144–2157 (2018).
29. P. Cheben, R. Halir, J. H. Schmid, H. A. Atwater, and D. R. Smith, "Subwavelength integrated photonics," Nature **560**, 565–572 (2018).
30. J. M. Luque-González, A. Sánchez-Postigo, A. Hadij-ElHouati, A. Ortega-Moñux, J. G. Wangüemert-Pérez, J. H. Schmid, P. Cheben, I. Molina-Fernández, and R. Halir, "A review of silicon subwavelength gratings: building break-through devices with anisotropic metamaterials," Nanophotonics **10**, 2765–2797 (2021).
31. N. Yang and J. Xiao, "A compact silicon-based polarization-independent power splitter using a three-guide directional coupler with subwavelength gratings," Opt. Commun. **459**, 125095 (2020).
32. H. Xie, J. Zheng, P. Xu, J. Yao, J. Whitehead, and A. Majumdar, "Ultra-compact subwavelength-grating-assisted polarization-independent directional coupler," IEEE Photon. Technol. Lett. **31**, 1538–1541 (2019).
33. X. Jiang and D. Dai, "Compact, broadband, and polarization-insensitive 3 dB power splitter on silicon," in *Asia Communications and Photonics Conference (ACP)* (2018), pp. 1–2.
34. T. Hao, A. Sánchez-Postigo, P. Cheben, A. Ortega-Moñux, and W. N. Ye, "Dual-band polarization-independent subwavelength grating coupler for wavelength demultiplexing," IEEE Photon. Technol. Lett. **32**, 1163–1166 (2020).
35. A. Herrero-Bermello, J. M. Luque-González, R. Halir, P. Cheben, A. Ortega-Moñux, I. Molina-Fernández, and A. V. Velasco, "Zero-birefringence silicon waveguides based on tilted subwavelength metamaterials," IEEE Photon. J. **11**, 2700308 (2019).
36. W. Zhong and J. Xiao, "Ultracompact polarization-insensitive power splitter using subwavelength-grating-based MMI couplers on an SOI platform," Appl. Opt. **59**, 1991–1997 (2020).
37. J. M. Luque-González, A. Ortega-Moñux, R. Halir, J. H. Schmid, P. Cheben, Í. Molina-Fernández, and J. G. Wangüemert-Pérez, "Bricked subwavelength gratings: a tailorable on-chip metamaterial topology," Laser Photon. Rev. **15**, 2000478 (2021).
38. R. Halir, P. Cheben, J. M. Luque-González, J. D. Sarmiento-Merenguel, J. H. Schmid, G. Wangüemert-Pérez, D.-X. Xu, S. Wang, A. Ortega-Moñux, and Í. Molina-Fernández, "Ultra-broadband nanophotonic beamsplitter using an anisotropic sub-wavelength metamaterial," Laser Photon. Rev. **10**, 1039–1046 (2016).
39. S. G. Johnson and J. D. Joannopoulos, "Block-iterative frequency-domain methods for Maxwell's equations in a planewave basis," Opt. Express **8**, 173–190 (2001).
40. A. F. Oskooi, D. Roundy, M. Ibanescu, P. Bermel, J. Joannopoulos, and S. G. Johnson, "Meep: a flexible free-software package for electromagnetic simulations by the FDTD method," Comput. Phys. Commun. **181**, 687–702 (2010).
41. A. Ortega-Moñux, J. Čtyroký, P. Cheben, J. H. Schmid, S. Wang, I. Molina-Fernández, and R. Halir, "Disorder effects in subwavelength grating metamaterial waveguides," Opt. Express **25**, 12222–12236 (2017).